



## Open Nanofluidic Films with Rapid Transport and No Analyte Exchange for Ultra-Low Sample Volumes

Journal:	<i>Lab on a Chip</i>
Manuscript ID	LC-ART-02-2018-000186.R2
Article Type:	Paper
Date Submitted by the Author:	10-Jun-2018
Complete List of Authors:	<p>Twine, Nicholas; University of Cincinnati College of Engineering and Applied Science, Electrical Engineering and Computer Systems; University of Cincinnati College of Engineering and Applied Science, Electrical Engineering and Computer Systems</p> <p>Norton, Ryan; University of Cincinnati College of Engineering and Applied Science, Electrical Engineering and Computer Systems</p> <p>Brothers, Michael; UES, Inc.; Air Force Research Laboratory, 711th Human Performance Wing</p> <p>Hauke, Adam; University of Cincinnati, Novel Devices Laboratory, Department of Electrical and Computer Engineering</p> <p>Gomez, Eliot; University of Cincinnati, Electrical Engineering and Computing Systems</p> <p>Heikenfeld, Jason; University of Cincinnati, Novel Devices Laboratory, Department of Electrical and Computer Engineering</p>

# Open Nanofluidic Films with Rapid Transport and No Analyte Exchange for Ultra-Low Sample Volumes

Cite this: *Lab Chip*, 2018, 00, 1

N. Twine<sup>1\*</sup>, R. Norton<sup>1</sup>, M. Brothers<sup>2</sup>, A. Hauke<sup>1</sup>, Eliot Gomez<sup>1</sup>, J. Heikenfeld<sup>1</sup>

Received 15th February 2018,

Accepted 00th May 2018

DOI: 10.1039/x0xx00000x

www.rsc.org/

Moving to ultra-low (<100 nL) sample volumes presents numerous challenges, many of which can be resolved by implementation of open nanofluidic films. These nanofluidic films are fabricated using a hexagonal network of gold-coated open microchannels which capture all of the following innovative advantages: (1) sample volumes of <100 nL/cm<sup>2</sup>; (2) zero analyte exchange and loss with the film materials; (3) rapid and omni-directional wicking transport of >500 nL/min per square of film; (4) ultra-simple roll-to-roll fabrication; (5) stable and bio-compatible super-hydrophilicity for weeks in air by peptide surface modification. Validation includes both detailed in-vitro characterization and in-vivo validation with sweat transport from the human skin. Sampling times (skin-to-sensor) of <3 min. were achieved, setting new benchmarks for the field of wearable sweat sensing. This work addresses significant challenges for sweat biosensing, or for any other nano-liter regime (<100 nL) fluid sampling and sensing application.

## Introduction

Transporting microliter sample volumes and coupling them to analyte sensing is now technologically mature, with applications spanning conventional lab-on-a-chip, to lateral flow-assays, to point of care applications. However, these present solutions for sample transport are often ill-equipped for the nanoliter regime (<100 nL) of sample transport and analyte sensing. Major challenges in the nanoliter regime include sensor integration, increased resistance to fluid flow, and prohibitive amounts of analyte exchange between the sample and the transport medium (Table 1). A particularly illustrative application example of these challenges is sweat biosensing<sup>1</sup>, where a significant advantage over other non-

invasive biofluids is the potential for continuous sensing (e.g. short lag time between unique data points). As an illustrative example of the challenge, consider recent work<sup>2</sup> in reducing sweat sample volume with an ~8 μL microchannel approach and a stated sweat collection area of ~0.1 cm<sup>2</sup> that would result in a ~8 hour collection time at a conventional sweat generation rate of ~1 nL/min/gland (e.g. frequently occurring natural rates<sup>3</sup>, or prolonged stimulation rates<sup>4</sup>). Alternately and differently challenged, consider wicking materials such as Rayon that have been demonstrated for sweat biosensing<sup>5</sup>. Rayon does have a potential smaller sample volume advantage by transporting fluid only along the wicking nano-grooves of the Rayon fiber. However, using Rayon and other polymers ignores the fact that even for high concentration analytes such as electrolytes (10's mM) the analyte exchange (loss) with the bulk Rayon material (regenerated cellulose) is so great that it makes it impossible to rapidly sense analyte concentration changes<sup>6,7</sup>. Other materials can be even worse,

**Tbl. 1** Comparison of fluid transport options in terms of major criteria that pose challenges for nL-regime sample volumes. X= disadvantage and ✓ = advantage.

Material	<100 nL/cm <sup>2</sup>	Surface Area	Analyte Exchange	Complexity
Glass channels	X / ✓	✓	✓	X
Paper	X	X	X	✓
Rayon / Fibers	✓	X	X	✓
Textured Surface	✓	X	✓	✓
Hex Wick (this work)	✓	✓	✓	✓

<sup>a</sup> Department of Electrical Engineering & Computer Science, University of Cincinnati, Cincinnati, OH, 45221, USA.

<sup>b</sup> Winkle College of Pharmacy, University of Cincinnati, Cincinnati, OH, 45267, USA.

<sup>c</sup> College of Nursing, University of Cincinnati, Cincinnati, Ohio, 45221

<sup>d</sup> UES, Inc., Dayton, Ohio 45432, USA. 711th Human Performance Wing, Air Force Research Laboratory, Wright-Patterson Air Force Base, Ohio, USA

† Electronic Supplementary Information (ESI) available: [details of any supplementary information available should be included here]. See DOI: 10.1039/b000000x/

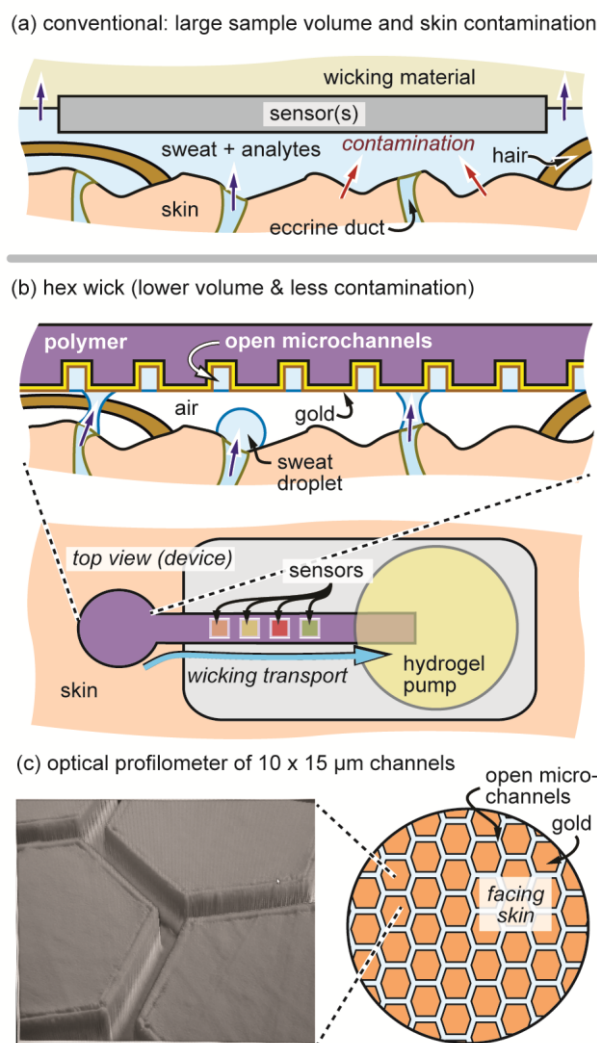


**Fig. 1** Approaches for sweat sampling **a**) conventional sensor-direct -on-skin with large sample volume with analyte contamination; **b**) hex wick (this work); **c**) optical profilometer image of 10x15 μm channels in the hex wick.

for example, widely utilized PDMS<sup>2,8</sup> will readily absorb hydrophobic small molecule analytes<sup>9,10</sup>, (e.g. hormones like Cortisol that are found in nM unbound concentrations<sup>1</sup>). These fundamental and significant challenges that cannot be ignored if continuous data with high temporal resolution (~e.g. minutes) is to be obtained for sweat biosensing, or for any other nano-liter regime fluid sampling and sensing application.

Reported here are open nanofluidic wicking films (hex wicks, Figure 1) with rapid transport (Figure 4), no analyte exchange, and both in-vitro (Figure 5 and 6) and in-vivo demonstrations (Figure 7 and 8) for sweat biosensing. These hex wicks address major challenges through a simple and elegant design that captures all of the following innovative features: (1) achieving an equivalent effective wicking film thickness of ~1 μm (<100 nL/cm<sup>2</sup>) by utilizing a hexagonal network of ~10x10 μm open channels that comprise ~10% of the open surface are (2)

eliminating analyte exchange with the bulk micro-replicated polymer material by use of a thin gold coating; (3) promoting rapid wicking transport through rectangular microchannels instead of a wicking surface or fibers which would impart greater drag force (Table 1); (4) using ultra-simple fabrication by roll-to-roll replication, enabled by the fault-tolerant nature of the open hexagonal network of channels (ability of fluid to re-route around manufacturing defects); (5) satisfying an operational need for super-hydrophilicity<sup>11</sup> by using a shelf-stable yet also biologically safe peptide approach for surface modification; (6) allowing omni-directional wicking beyond corner junctions by achieving stable hydrophilicity of the films, which is unlike more-limited linear wicking capability of commercial films like the 3M MSX 7250. Specifically, for sweat biosensing, the hex wick also reduces the dead volume against the skin surface (Figure 1b), which brings an added advantage of reducing analyte exchange with the stratum corneum<sup>12</sup>.

This paper begins with the theoretical and design criteria for hex wicks, including important calculations that drive the need for super-hydrophilicity. Next the fabrication processes are described, including roll-to-roll fabrication results that confirm allowance of non-ideal corner-rounding. In addition, a novel, robust, and biocompatible peptide surface hydrophilization method is demonstrated which could also have impact on other biotechnologies. Next, in-vitro testing is performed accounting for basic wicking capacity and speed, and in terms of the wicking pressures required for sweat biosensing applications. Then, in-vivo validation is performed that show the films can wick sweat from skin to electrodes (mock sensors) in mere minutes. Lastly, several future challenges are discussed related to advanced sensor integration. This work addresses major challenges that cannot be ignored if useful data is to be obtained for sweat biosensing, or for other nano-liter regime (<100 nL) fluid sampling and sensing application.

## Hex Wick: Design and Theory

### Consideration of Conventional Approaches

Before commencing this work, several prior-art approaches were first considered through a thought-experiment framework (Table 1). Glass/silicon channels were considered due to the promise of low sample volumes (<100 nL) but were not pursued because of the complexity of integrating sensors using monolithic microfabrication. Paper is an obvious initial choice, used routinely in lateral flow assays, but has too great of a thickness (~100 μm, large volume) and has a significant surface area (drag forces, non-specific absorption) and has the potential confounding factor of significant analyte exchange into and out of cellulose itself.

## Lab on a Chip

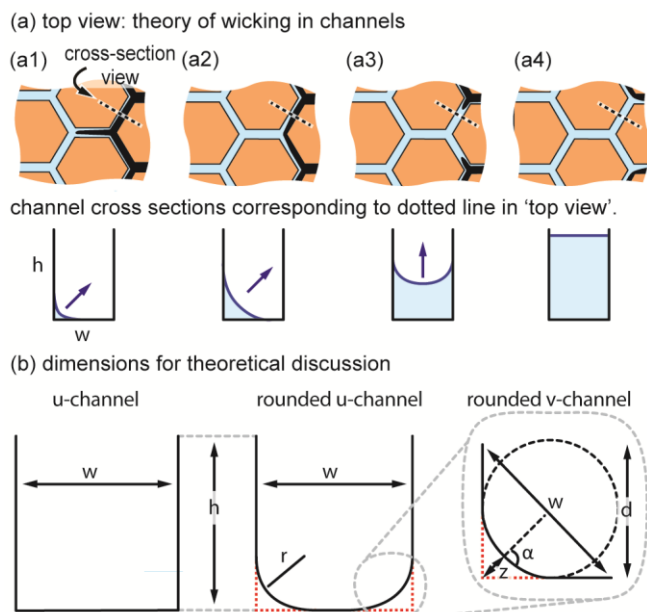


**Fig. 2** Theoretical framework of fluid flow in a hex wick **a)** top-view of hex wick with respective side-view of a channel filling representing the dotted-line shown in the top-views; **b)** dimensions governing fluid transport.

Replacing paper with a wicking material that only wicks along the fibers in the material, such as Rayon, solves sample volume issues (wicking volume is <10% of its thickness), but surface area and analyte exchange remain major issues even for high-concentration electrolytes<sup>6,7</sup>. A textured super-hydrophilic surface does reduce the sample volume and can also be metal-coated to prevent analyte exchange<sup>13</sup>, but requires a very high surface area to volume ratio (fluid drag, non-specific absorption). For all these reasons, instead a hexagonal network of open surface channels (hex wick) was pursued to satisfy all the critical criteria (Table 1): ultra-low volumes, minimum surface-area to volume, no analyte exchange, and simplicity. Other channel network geometries (square, triangular, etc.) are theoretically possible<sup>14</sup>, but we currently see no compelling advantages over a hexagonal network that minimizes the number of channels that must intersect at each junction. To elaborate on simplicity, once large sheets of hex wicks are fabricated, they can simply be cut to size and laminated against other components such as sensors (Figure 1b) and/or other hex wicks to build up a functional device.

### Theoretical Design Requirements

The mechanics for fluid transport in the hex wick are more sophisticated than one might expect, especially since they rely on open microfluidic channels with divergent capillary dimensions at the connecting junctions<sup>14–17</sup>. Multiple wicking principles are required for the hex wick and are described here in the order of difficulty to achieve a continuous wicking process (Figure 2): 1) capillary flow in an open u-channel with

perfect corners; 2) capillary flow in an open u-channel with *rounded corners*; 3) capillary filaments propagating along rounded corners (rounded v-channels).

Capillary flow in an open u-channel (Figure 2b) can be modeled as a combination of two v-grooves. The u-channel corner-wicking in its simplest explanation is determined by the channel aspect ratio's ( $w$ ) and length ( $l$ ) and Young's contact angle, ( $\theta$ ). For an open u-channel with perfectly sharp corners, the condition for capillary flow is<sup>14</sup>:

$$\frac{w}{2h + w} < \cos\theta \quad (1)$$

thus, for an aspect ratio of 1.5 (10  $\mu\text{m}$  width and 15  $\mu\text{m}$  height) the contact angle necessary to satisfy capillary flow is <75°. Maintaining this low of a contact angle is trivial, but a major challenge is that real world fabrication methods will likely have corner rounding with a radius ( $r$ ), resulting in a more challenging condition for capillary flow<sup>14</sup>:

$$\underbrace{\frac{w}{2h + w}}_{\text{theoretical}} + \underbrace{\frac{wr(4 - \pi)}{2h + w^2}}_{\text{corner-rounding}} < \cos\theta \quad (2)$$

Using Equation 2, and even a worst-case corner rounding with a radius equal to the width of the channel of 10 $\mu\text{m}$ , the contact angle necessary for capillary flow to occur is 66°, also trivial to achieve with many hydrophilic materials. However, because the hex wick is hexagonal network with divergent capillary geometries at the channel junctions, a third and most difficult requirement exists: unless more difficult-to-make high-aspect-ratio channels are utilized, capillary filaments along the corners are necessary to promote continuous wicking. The requirement for capillary filaments is best understood by discussion of the wicking processes illustrated in Figure 2a.

Fluid in the hex wick propagates in a repeating pattern described in the 4 main steps shown in Figure 2 a1-a4: (a1) - a capillary filament occurs at the corners of the channels, and travels ahead of the bulk capillary flow; (a2) - this capillary filament in the corner has a concave meniscus and therefore due to Laplace pressure also continues to fill the corner; (a3) - eventually the capillary filament reaches the other channel side wall, and a new concave meniscus is formed which then further fills the channel due to Laplace pressure; (a4) - this filled channel then supports flow toward additional capillary filaments and channel filling. In the hex wicks reported here (see online supplementary video) the capillary filaments propagate so quickly that they surround an entire hexagon perimeter before channel filling occurs. It should be noted that although the maximum volume of the hex wick is ~150nl/cm<sup>2</sup> (10x15  $\mu\text{m}$  channels, 10% of surface area), during use with a hydrogel or cellulose pump (Figure 1b) it is unlikely the channels will be fully filled, and the volume during use is likely <100 nL/cm<sup>2</sup> (see In-Vitro Validation section).

The need for the capillary filaments presents a major challenge that impacts materials of choice. A spontaneous

capillary filament can be understood by representing the corners of the channels as rounded v-grooves with the dimensions shown in Figure 2b, and theoretically modeled as<sup>14</sup>:

$$\sin\alpha\left(1 + 2\alpha\frac{z}{w}\right) < \cos\theta \quad (3)$$

Using the same numbers described previously, and assuming a corner rounding radius of 1  $\mu\text{m}$ , the necessary contact angle is  $<35^\circ$ . This presents a major challenge in materials selection, as will be discussed next.

## Hex Wick: Microfabrication

Initial proof of concept was performed using a conventional PDMS cast and cure process on SU-8 molds. The PDMS was hydrophilized with plasma treatment. We mention this approach, because although PDMS fails many of our application requirements (see Introduction), it will allow researchers a rapid method for initially evaluating the wicking-performance of hex wicks. We now describe the robust and scalable microfabrication technique which meets our application requirements, and which was used for all experiments reported herein.

### Roll-to-Roll Microreplication

SU-8 microfeatures were patterned on a silicon wafer to create a master mold. The features consisted of  $10 \times 15 \mu\text{m}$  walls, and empty hexagonal shapes. This master mold was shipped to Wave Front Technologies Inc. where they implemented a proprietary UV cast-and-cure roll-to-roll compatible micro replication process in polymer (Figure 3a, 3b). Because the polymer is gold-coated, any polymer will suffice so long as it allows gold-adhesion and it satisfies the geometrical requirements (see Design and Theory section).

### Surface Modification with Gold and Thiols

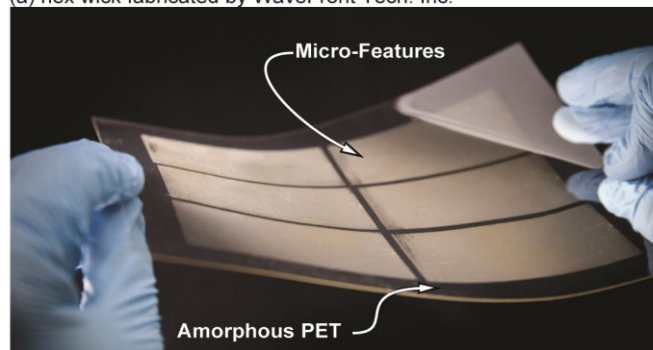
As described in the Design and Theory section, a very low water contact angle of  $<35^\circ$  is required for capillary filaments to propagate along even rounded corners in the hex wick channels. Textured surfaces can be used reduce the apparent contact angle but were not utilized here because they fail our requirement of minimizing surface area (Design and Theory section, Table 1).

We further desired an approach that would be compatible on a sputter-deposited 10 nm gold coating, because this gold coating would block all analyte exchange with the microreplicated polymer. We therefore focused on thiol functionalization<sup>18</sup>, but with yet another added requirement: biological compatibility and potential classification of being generally regarded as safe (GRAS) with skin contact in sweat biosensing applications (Figure 1b).<sup>1</sup> Even though arguably the thiols

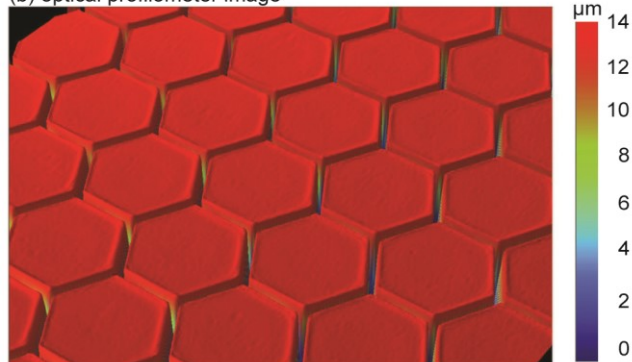
would be bound to the gold which could prevent biocompatibility issues, we ensured the thiols which were inherently GRAS even if they released from the gold.

## Lab on a Chip

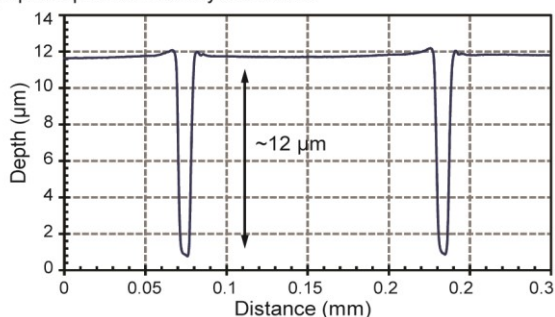
(a) hex wick fabricated by WaveFront Tech. Inc.



(b) optical profilometer image



(c) optical profilometer x-y scan data



(d) thiol stability - materials for hydrophilization

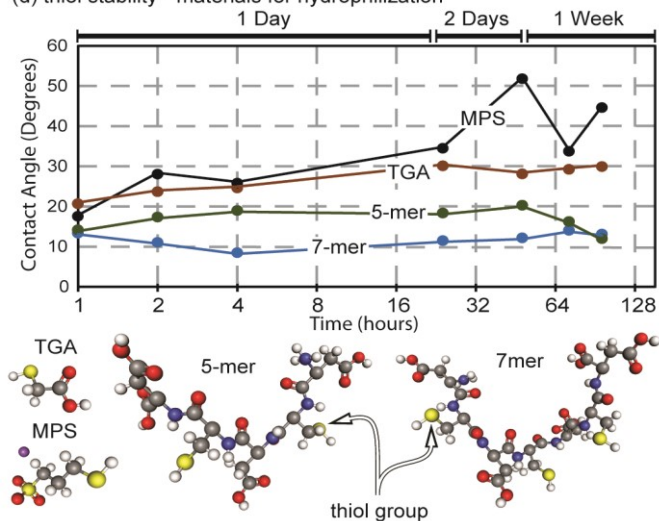


**Fig. 3** Materials used in fabrication of hex wick **a)** roll-to-roll fabricated sheet of hex wick; **b)** 3D optical profilometer image of hex wick; **c)** surface profile of typical microfeatures; **d)** plot showing week-long stability of the various thiols in air (VCA Optima System).

Our initial attempts focused on a monothiol thioglycolic acid (TGA) which is used in hair straightening products, and therefore likely meets the biocompatibility requirement. For comparison, another monothiol sodium 3-mercapto-1-propanesulfonate (MPS) was explored. MPS (T3758, CAS 68-11-1, 90% purity) and TGA 251682, CAS 17636-10-1 98% purity) were purchased from Sigma Aldrich (St. Louis, MO). Gold coated samples were soaked in 30 mM thiol solutions containing 1 x PBS for 10 minutes and then dried with nitrogen. Sodium hydroxide was added as necessary to deprotonate the carboxylic acid groups to form the charged carboxylate, simultaneously enhancing solubility and increasing the electrostatic forces between the thiol solutions and water. Both TGA and MPS were shown to initially meet our  $<30^\circ$  contact angle requirements, but both showed a

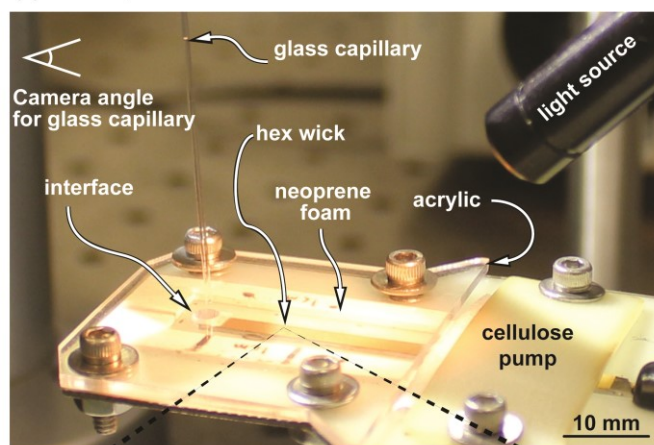
gradual increase in contact angle over time (~1 week). 1 week is certainly long enough for experimentation, but for real applications, shelf-stability is ultimately required. We speculate that contact angle increase is due to gold oxidation which can de-bond the thiol linkage (Figure 3d). We therefore explored agents with multiple thiol bonding to the gold to improve resilience to debonding<sup>19</sup> (if one thiol bond is lost, the others remain in place, further allowing the lost thiol bond to even potentially reform). Unfortunately, few solutions exist which would be regarded as GRAS, such as lipoic acid; additionally, the charge density of lipoic acid is poor: 1 charged moiety for every 206 Da. We therefore leveraged small peptides which have potential to meet our GRAS requirement, specifically implementing 5mer (2 cysteine groups, dithiol) and 7mer (3 cysteine groups, tri-thiol) peptides. Cysteine residues have a propensity to form a beta-sheet, where the side-chains are on the same side in alternating residues<sup>20</sup>. In this study, we incorporated aspartic acid for the amino acid to improve hydrophilicity due to its low molecular weight, as well as its indifference to forming a beta-sheet secondary structure that we believe will enhance the stability of binding<sup>20</sup>. The peptides were purchased from Genscript (Piscataway, NJ, 95% purity) and applied by resolubilizing into 1X PBS with addition of sodium hydroxide to deprotonate the carboxylic acid groups to make a 30 mM solution. This solution was then applied onto the gold substrate for 10 min. As shown in Figure 3d, these peptides impart impressively low and stable contact angles, which we believe is in large part to the density of charged moieties (114 Da/ charged moiety for the 5mer, 131 Da/charged moiety for the 7mer). During later experiments (next sections), hex wick samples with 5mer and 7mer functionalization, even stored in air for weeks, functioned normally. For all thiols, we also confirmed stability in nitrogen gas (i.e. shelf storage in a sealed foil pouch) and in a solution of pH ~ 5.6 which is similar to sweat (see online supplementary material). This gold/peptide approach for robust<sup>21</sup> and biocompatible hydrophilization is an innovation that may prove useful to other applications of microfluidics and biotechnology. Assuming a 10 degree contact angle (7mer, Figure 3d), we calculate that the capillary pressure of the wetted hex-wick (u-channel filling) to be ~10 kN/m<sup>2</sup>.

## In-Vitro Validation

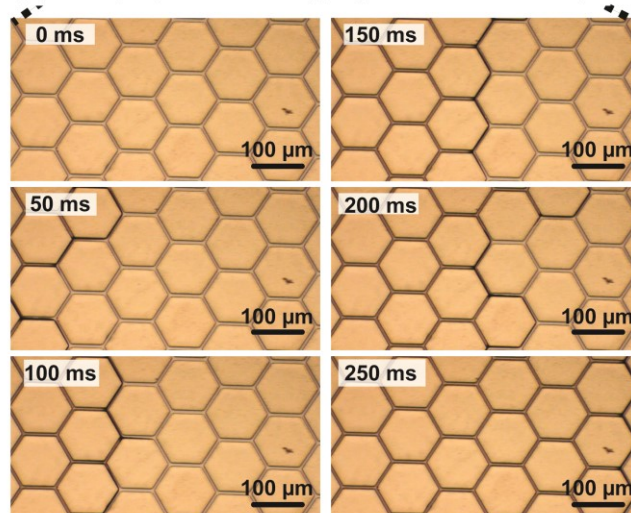
In this section, testing of the wicking capacity was performed along with microscopy of the wicking to confirm the operational theory of fluid propagation (see Design and Theory). Also, an in-vitro validation with artificial sweating skin was performed to further demonstrate both wicking capacity and wicking pressure.

### Wicking Capacity of Stand-Alone Channels

(a) test setup



(b) time-lapse photos of wicking progress under a microscope



(c) plots of wick rate vs. aspect ratio

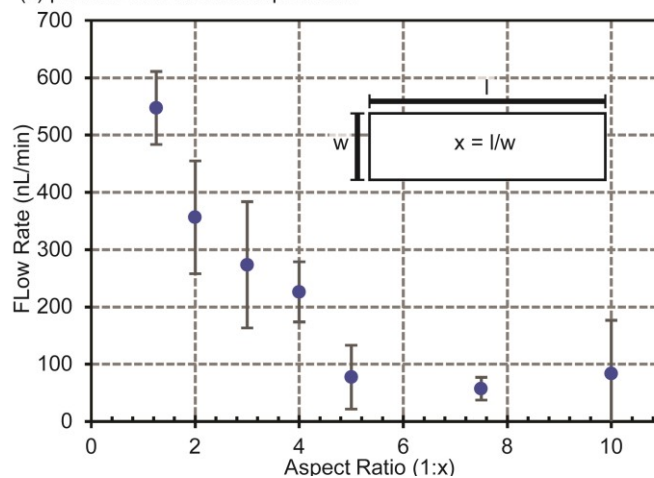


**Fig. 4** Setup for in-vitro characterization of flow rate through the hex wicks; **a)** test setup; **b)** capillary flow through the wick under the microscope; **c)** plot of flow rate vs. film aspect ratio.

Developing a testing setup for wicking capacity required a sophisticated setup, because when moving to such small sample volumes and an open nanofluidic device like the hex wick, water evaporation is a major challenge as it

## Lab on a Chip

can easily dominate over wicking. As shown in Figure 4a-b, an acrylic viewing port was placed over the sample to be tested and viewed under a camera. The base of the setup is a garolite board that is laser cut. One sixteenth in. thick neoprene foam with an adhesive backing (McMaster-Carr) was attached to the garolite board to make a foam seal that would surround the hex wick sample on its sides to further prevent evaporation. Conventional syringe pumps fail to provide reliable control at the ultra-low sample volumes tested in this work, so a 0.4 mm inner diameter glass capillary tube was placed at the inlet and coupled to the hex wick with a 2 x 2 mm sheet of TechniCloth (TX609, 55% Cellulose, 45% Polyester, Kernersville North Carolina). The capillary tube is dimensionally an order of magnitude larger than the hex-wick's effective capillary dimensions, and therefore can be approximated as a non-factor. The Techni-Cloth, once saturated, has no wicking pressure. Hence, we assume that wicking performance is dominated by the hex-wick itself. The rate of fluid introduction could then be measured by a camera which visually captured at 30s intervals the decrease in height of the column of water in the capillary tube. A folded piece of paper towel (cellulose pump) was clamped against the other end of the test setup to act as a wicking outlet (waste reservoir). Videos corresponding to the photos show in Figure 4b are available with the online supplementary material. If the reader views the videos on a large screen they might be able to notice capillary filaments (corner wicking) proceeding ahead of the channel wicking, as previously described and shown in Figure 2. Flow rates over 500 nL/min were observed for hex wicks with a film width to length aspect ratio of 1:1 (Figure 4c). As the length of the wick increased the flow rates slowed down but maintained approximately 100 nL/min flow rates even at high film aspect ratios (10:1) (Figure 4c).

### Testing on Artificial Skin

An additional application-oriented in-vitro test of the hex wick was performed for wicking of sweat off of artificial microfluidic skin. This test further validates wicking capacity and demonstrates that the hex wick can void a hydrophilic cavity of a fluid by having a strong drawing wicking force. This functionality is particularly important to sweat biosensing where removing sweat quickly from the skin surface can minimize contamination from, and analyte exchange with, the stratum corneum<sup>12</sup>(Figure 1a,b).

The artificial skin was fabricated, and the hex wick in-vitro tested using water with green fluorescent dye, and 494 nm excitation light, as previously reported by our group<sup>12,22</sup>. The interfacing of the hex wick with the artificial skin is illustrated in the side-view diagram of Figure 5 and top view diagram and time-lapse photos are shown in Figure 6. A paper pump was again utilized and

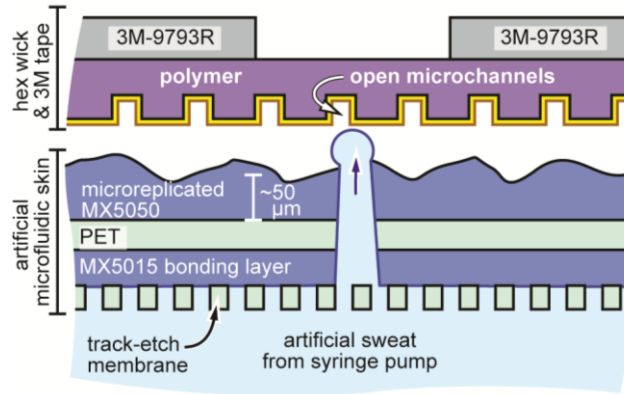


**Fig. 5** In-vitro artificial skin diagram of in-vitro test setup with artificial microfluidic skin.

connected to a 10 mm extension of the wick which is not shown (would be to the right-side of diagram 6a and photos 6b-6o). The ~10 nm gold coating is thin enough that it is partially transparent to both the excitation light and fluid fluorescence. In Figure 6c, the first fluid introduction (initial wetting) involves wicking along the bottom of the grooves in the artificial skin (faint green fluorescent lines) which is nearly completing as visualized by the white dotted lines and arrows.

These are indeed the bottoms of grooves and not wicking between the hex wick and the tops of skin ridges because these same faint green lines are a stronger in green color when fully covered with the fluid (i.e. thicker fluid layer, more fluorescence, e.g. Fig. 6m). As shown in Figures 6e, 6j, 6m fluorescein dye was injected periodically in 2  $\mu$ L pulses (kdScientific 110 syringe pump and a Hamilton 80222 syringe) and then allowed to recover over a period of ~4-5 minutes (~400-500 nL/min). The height between the artificial skin and hex wick clearly varies over several hundred  $\mu$ m and each initial volume of fluid wicks by capillary action to the edges where the height is lesser (obvious by fluorescent intensity and variable area of the 2  $\mu$ L of fluid). The hex wicks tested in Figure 6 roughly correspond to film aspect ratios of ~1:1 to ~1:2 and the flow rate results are in general agreement with the results of Figure 4c. Videos corresponding to the photos shown in Figure 6 are available with the online supplementary material. If the reader views the videos

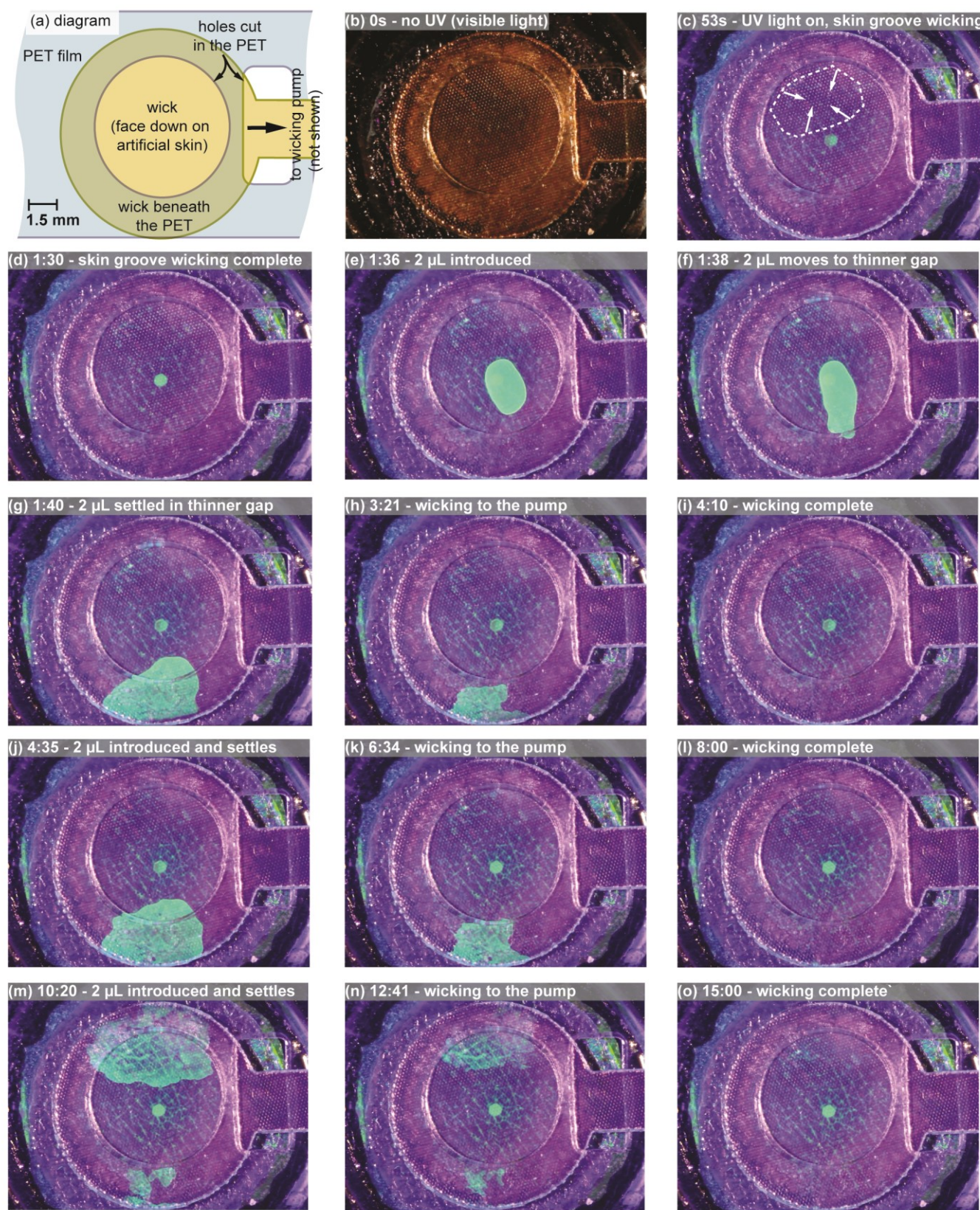


**Fig. 6** Testing on artificial skin including (a) diagram and (b)-(o) photographs labeled with time-stamps.

## Lab on a Chip

on a large screen they will also notice a corresponding fluorescent intensity change for the channels in the hex wick, showing that the paper pump empties most of the channel unless the hex wick is flooded with new fluid. This supports our hypothesis that below the wicking capacity (Figure 4c), the wicking volume of the hex wick is likely far below the maximum wicking volume of 150 nL/cm<sup>2</sup>. In summary, the results of Figure 6 clearly confirm the wicking capacity of the hex wicks (Figure 4c) and the ability to void the space between hex wicks and a skin surface (Figure 1b).

## In-Vivo Validation

Human subjects testing was performed under the guidance of the University of Cincinnati's (UC) Human Research Protection Program (ID# 2016-4386 approved by the UC Institutional Review Board). All human subjects provided informed consent.

Fabrication of the device occurred the day before the experiment including screen printing a 5-electrode system on 3 mil PET, fabricating the hex wick, and device assembly (adhesives, cables, etc.). The assembly and placement on real skin was similar to that used for the artificial skin (Figure 6a). One electrode (the reference) was printed in Ag/AgCl (CL-4001, Engineered Conductive Solutions, Delaware, Ohio), and the rest were printed in carbon ink (CI-2001, Engineered Conductive Solutions, Delaware, Ohio), all with a width of 0.4 mm and separation distance of 1.8 mm. The hex wick touching the skin was 11 mm in diameter and the wick laying across the sensors was 4 mm wide. To couple the electrode sensors to the hex wick, 1.5 mm by 6 mm strips of 100  $\mu$ m thick Rayon were laid directly onto the screen-printed electrodes (Figure 7a). These five Rayon strips should combine for a total fluid capacity of  $\sim$ 270 nL (based on estimated 6% of total volume). As discussed in the introduction, Rayon is ultimately not an ideal choice for fluidic coupling, and hydrogels or other materials may be preferred (see next Discussion section).

A single-sided 3M tape of 5 cm diameter was then used to enclose the entire system, to eliminate evaporation, and to adhere the device to skin. Because in this in-vivo test, the hex wick has very strong wicking pressure, capillary wicking between the hex wick and underlying PET substrate has little or no significance on the total device fluidic volume. This is because the electrodes and Rayon on the PET separate the hex wick from the PET by a  $>100$   $\mu$ m air gap (weaker wicking pressure). Alternate approaches for thinner sensors, which might not have a substantial air gap, could include a super-hydrophobic coating on the PET substrate.

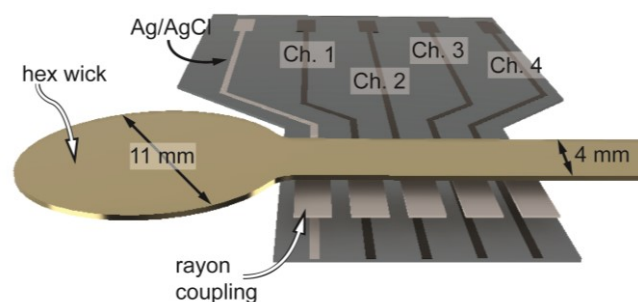
A cable was then connected to the screen-printed electrode leads using z-axis conductive tape and connected to a multipurpose electrochemical unit (PalmSens3, PalmSens BV, Houten, Netherlands). Chrono

potentiometric measurements were cycled through each of the 4 carbon electrodes by the Ag/AgCl electrode as the reference at 1 nA constant current.

Sweat stimulation was performed as follows. Carbachol gel discs (3% agarose, 1% Carbachol) were fabricated as previously reported by our group<sup>4,23</sup>. The human subject's arm was wiped with a paper towel wet with IPA, then a paper towel wet with DI water. This was repeated 3 times. Then the electrodes were wet with deionized water and the gel discs (15 mm diameter) were placed on the arm. Carbachol was then delivered iontophoretically into the skin for 75 s with a total dose of 37.5 mC. The subject's arm was then dried with a paper towel. Then, one hour after the time of stimulation, the stimulated area was wiped dry with a paper towel, and immediately, a 17mm diameter wipe (2.26 cm<sup>2</sup>) was placed on the stimulated site under light pressure from an acrylic holder<sup>4</sup>. After 10 minutes the paper disc was removed and the increased weight change was measured gravimetrically and translated into sweat generation rate<sup>4</sup>. Calculations of sweat rate using the gravimetric data and the subject's gland density provided an accurate verification of actual sweat generation rates<sup>4</sup>: 2.32 nL/min/gland for subject 1 (Figure 8a), and 2.45 nL/min/gland for subject 2 (Figure 8b).

As shown in Figure 8, after drying the skin and immediately applying the test device (Figure 7), each of

(a) diagram of in-vivo test setup



(b) photo of experimental setup on test subject

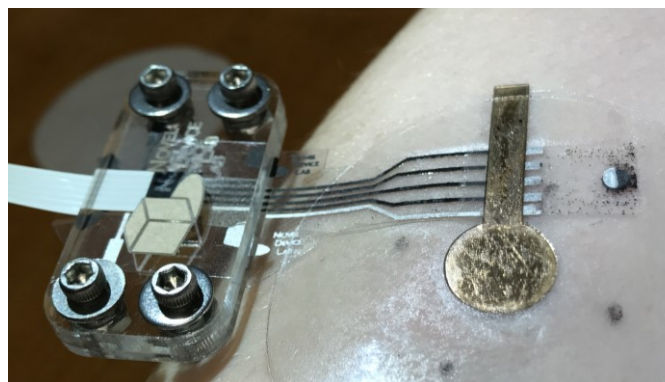


**Fig. 7** Human-subject testing on real skin including (a) diagram and (b) photographs of the test-setup.

the 4 sensor electrode channels were measured for when sweat initially reaches it by a change in potential at the electrode from a floating potential of  $-5$  V to a potential of  $0$  V vs. the Ag/AgCl reference (note in Figure 8 that the Ag/AgCl reference was the first electrode placed in the fluid flow path such that it would already be in contact with sample before the working electrodes). As the first electrode (Ch. 1) responds, the voltages for other electrodes shift as well due to minor cross-coupling of voltages to the floating electrodes. As shown in Figure 8, it is clear that the electrodes all responded in less than 3 minutes, which are the fastest sweat-to-sensor transport times to the best of our knowledge.

The results of Figure 8 also correlate to what we would expect theoretically. The stimulated area on skin was  $15$  mm, yielding an area of  $1.76$  cm<sup>2</sup>. This is larger than that of the hex-wick, and some additional sweat could be pushed under the adhesive outside the hex wick. However, that is unlikely to be significant during the short time-scales tested here, (Figure 8) nor strongly impact the following theoretical calculations.

The hex wick used here has  $10 \times 15$   $\mu\text{m}$  channels at 10% of the area, and therefore  $\sim 150$  nL/cm<sup>2</sup> maximum volume. So, the actual  $0.95$  cm<sup>2</sup> collection area channel volume can be calculated as  $145$  nL. A sweat generation rate of approximately  $500$  nL/min/cm<sup>2</sup> was measured gravimetrically by the disk wipes. Thus, sweat is wicked from a  $0.95$  cm<sup>2</sup> skin area that is generating  $475$  nL/min, and the  $145$  nL fluid capacity of the collection area channels should fill in  $\sim 18$  s. Next, consider the maximum volume of the remainder of the hex wick to be  $60$  nL and, as explained previously, the total wicking volume of the rayon strips on the electrodes to be  $270$  nL. The total volume is therefore  $475$  nL and, given the  $475$  nL/min sweat generation rate, the sensors should all respond within approximately  $1$  min of application to the skin. The additional delay between this theory and the experimental results (Figure 8) might be due to skin-groove wicking as observed in-vitro testing (Figure 6 and related discussion), and/or a potential air gap above sweat pores that must be bridged by sweat before wicking can commence.

## Discussion on Sensor Integration

Sensor integration remains a major challenge and topic of ongoing work for our research group. There are several challenges that effect sensor integration, especially electrochemical sensors. These challenges all stem from the fact that a sensor tested in large beaker of fluid (e.g. infinite fluid volume) is unlikely to give similar results in a much more confined environment with a much smaller fluid volume.

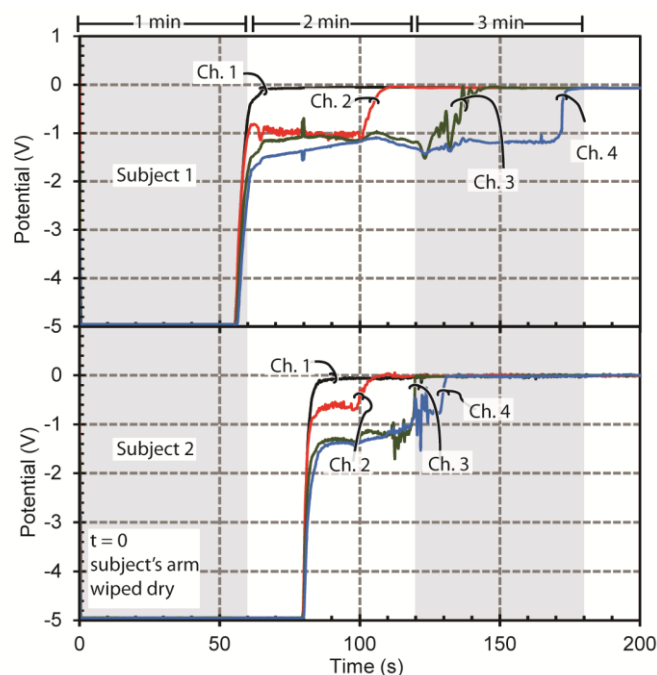


**Fig. 8** Electrode channel measurements vs. time for human-subject testing of (top) subject 1 and (bottom) subject 2. As each channel's potential changes to  $0$  V, it indicates that associated working electrode has been initially wetted and is fluidically coupled to the reference electrode via sweat.

### Fully Wetting the Sensor

Firstly, the sensor, like in a beaker, should be kept fully wet. Here we simply used Rayon to couple the hex wick to an electrode surface, but such an approach only has fluid contact where Rayon fibers touch the electrode. The Rayon will not become fully saturated with fluid between its fibers because of the needed influence of the hydrogel or paper pump (Figure 1b) which has the highest wicking pressure of any wicking element in the system. Any reduction in fluid contact area with a sensor can diminish its electrochemical signal, and therefore give a false reading dependent not on the amount of analyte present but rather the current amount of surface wetting of the sensor. Not only could this amount of surface wetting of the sensor change with incoming fluid flow rate, but for wearable sensors<sup>24</sup> mechanical motion/noise could change the surface wetting and make it extremely difficult to obtain quality sensor data. Therefore, a method such as hydrogel coupling of the sensor to the wick may resolve this issue, if such an approach can be shelf-stable, and if the thickness of the hydrogel can be low enough ( $10$ 's  $\mu\text{m}$  at most) such that it does not compromise the low-sample-volume advantage of the hex wick. A hydrogel or other type of coupling method is also beneficial, as it can help prevent potential electrical shorting between a sensor and the gold-coated hex-wick.

## Lab on a Chip

## Analyte Depletion

Secondly, in a confined environment for both enzymatic and affinity-based sensors, with a constrained sample volume, the sensor could locally deplete the analyte from the incoming solution, causing a false low reading of analyte concentration. For example, consider an aptamer-based electrochemical sensor<sup>25</sup> with  $\sim 10^{10}$  to  $10^{11}$  total analyte probes on a small 2 mm diameter electrode. For a 10 nM analyte concentration it would require a relatively (for the hex wick) huge sample volume of 10  $\mu$ L to have a comparable  $6.02 \times 10^{10}$  number of analytes available in the sample fluid. Therefore, if low sample volumes are to be preserved, in some cases for low concentration analytes, longer sensing times need to be allowed, or much smaller sensors need to be implemented (decreased total number of analyte probes).

## Electromagnetic Interference

Lastly, it is clear from the above discussion, that miniaturizing the sample volumes also means miniaturizing the sensing modality as well. For electronic sensors this could be problematic as the sensor electrical impedance is increased which increases susceptibility to external electromagnetic interference. Also, in wearable applications<sup>24</sup> this increases susceptibility to mechanically-induced electrical noise. Fortunately, the hex wick brings an inherent advantage with respect to electromagnetic noise, as it is metal coated and will act as at least a partial electromagnetic shield to external electromagnetic noise.

## Acknowledgements

The authors acknowledge support from the National Science Foundation and the industrial members of the Center for Advanced Design and Manufacturing of Integrated Microfluidics (NSF I/UCRC award number IIP-1362048), the Air Force Research Labs Award #USAF contract # FA8650-15-C-6625, NSF EPDT Award #1608275, and the Ohio Federal Research Network (PO FY16-049; WSARC-1077-700). The authors also would like to extend our thanks Dr. Leanna Levine from CADMIM and Chris Rich from WaveFront Technology.

## Competing Financial Interests

The corresponding author (Heikenfeld) also discloses a potential conflict of interest as he is a co-founder of Eccrine Systems Inc. which is commercializing sweat sensing technologies.

## References

- 1 J. Heikenfeld, *Electroanalysis*, 2016, 28, 1242–1249.
- 2 A. Martín, J. Kim, J. F. Kurniawan, J. R. Sempionatto, J. R. Moreto, G. Tang, A. S. Campbell, A. Shin, M. Y. Lee, X. Liu and J. Wang, *ACS Sensors*, 2017, 2, 1860–1868.
- 3 N. A. S. Taylor and C. A. Machado-Moreira, *Extrem. Physiol. Med.*, 2013, 2, 1.
- 4 P. Simmers, S. K. Li, G. Kasting and J. Heikenfeld, *J. Dermatol. Sci.*, 2017, 89, 40–51.
- 5 W. Gao, S. Emaminejad, H. Y. Y. Nyein, S. Challa, K. Chen, A. Peck, H. M. Fahad, H. Ota, H. Shiraki, D. Kiriya, D. H. Lien, G. A. Brooks, R. W. Davis and A. Javey, *Nature*, 2016, 529, 509–514.
- 6 S. Rebouillat and F. Pla, *J. Biomater. Nanobiotechnol.*, 2013, 04, 165–188.
- 7 S. Sen, J. D. Martin and D. S. Argyropoulos, *ACS Sustain. Chem. Eng.*, 2013, 1, 858–870.
- 8 A. Koh, D. Kang, Y. Xue, S. Lee, R. M. Pielak, J. Kim, T. Hwang, S. Min, A. Banks, M. C. Manco, L. Wang, K. R. Ammann, K. Jang, S. Han, R. Ghaffari, U. Paik, M. J. Slepian, Y. Huang and J. A. Rogers, *Sci Transl Med*, 2017, 8, 1–14.
- 9 J. D. Wang, N. J. Douville, S. Takayama and M. Elsayed, *Ann. Biomed. Eng.*, 2012, 40, 1862–1873.
- 10 M. W. Toepke and D. J. Beebe, *Lab Chip*, 2006, 6, 1484.
- 11 J. Drelich and E. Chibowski, *Langmuir*, 2010, 26, 18621–18623.
- 12 R. Peng, Z. Sonner, A. Hauke, E. Wilder, J. Kasting, T. Gaillard, D. Swaille, F. Sherman, X. Mao, J. Hagen, R. Murdock and J. Heikenfeld, *Lab a Chip - Miniaturisation Chem. Biol.*, , DOI:10.1039/C6LC01013J.
- 13 A. Hauke, L. S. S. Kumar, M. Y. Kim, J. Pegan, M. Khine, H. Li, K. W. Plaxco and J. Heikenfeld, *Biosens. Bioelectron.*, 2017, 94, 438–442.
- 14 J. Berthier, K. Brakke and E. Berthier, *Open Microfluidics*, Scrivener Publishing LLC; John Wiley & Sons, 2016.
- 15 I. Publishing, J. Berthier, D. Gosselin, N. Villard, C. Pudda, F. Boizot, G. Costa and G. Delapierre, 2014, 183, 123–128.
- 16 J. Berthier, K. A. Brakke, D. Gosselin, F. Navarro, N. Belgacem, D. Chaussey and E. Berthier, *Med. Eng. Phys.*, , DOI:10.1016/j.medengphy.2017.05.005.
- 17 J. Berthier, K. A. Brakke, D. Gosselin, M. Huet and E. Berthier, *AIMS Biophys.*, 2014, 1, 31–48.
- 18 C. Vericat, M. E. Vela, G. Benitez, P. Carro and R. C. Salvarezza, *Chem. Soc. Rev.*, , DOI:10.1039/b907301a.
- 19 N. Phares, R. J. White and K. W. Plaxco, *Anal. Chem.*, 2009, 81, 1095–1100.
- 20 T. B. of R. of the U. of W. System, Biological Magnetic Resonance Data Bank, <http://www.bmrb.wisc.edu/featuredSys/dhfr/index.shtml>, (accessed 1 January 2016).
- 21 Y. Xue, X. Li, H. Li and W. Zhang, *Nat. Commun.*, , DOI:10.1038/ncomms5348.
- 22 L. Hou, J. Hagen, X. Wang, I. Papautsky, R. Naik, N. Kelley-Loughnane and J. Heikenfeld, *Lab Chip*, , DOI:10.1039/c3lc41231h.
- 23 Z. Sonner, E. Wilder, T. Gaillard, G. Kasting and J. Heikenfeld, *Lab Chip*, , DOI:10.1039/C7LC00364A.
- 24 J. Heikenfeld, A. Jajack, J. Rogers, P. Gutruf, L. Tian, T. Pan, R. Li, M. Khine, J. Kim, J. Wang and J. Kim, *Lab Chip*, , DOI:10.1039/C7LC00914C.
- 25 N. Arroyo-Currás, J. Somerson, P. A. Vieira, K. L. Ploense, T. E. Kippin and K. W. Plaxco, *Proc. Natl. Acad. Sci.*, 2017, 114, 645–650.